IEEE Access
Multidisciplinary | Rapid Review | Open Access Journal

Received August 27, 2019, accepted September 12, 2019, date of publication September 20, 2019, date of current version October 1, 2019.

*Digital Object Identifier 10.1109/ACCESS.2019.2942687*

# Design of Broadband Compressed Sampling Receiver Based on Concurrent Alternate Random Sequences

**PENG WANG, FEI YOU, (Senior Member, IEEE), AND SONGBAI HE, (Senior Member, IEEE)**
School of Electronic Science and Engineering, University of Electronic Science and Technology of China, Chengdu 611731, China

Corresponding author: Fei You (feiyou@uestc.edu.cn)

This work was supported by the National Natural Science Foundation of China under Grant 61571080.

**ABSTRACT** Modulated wideband converter (MWC) is a multi-branch sub-Nyquist sampling structure for processing the spare wideband signals. By mixing with a periodic pseudo-random bit sequence (PRBS), each branch of MWC compresses the information of the input signal into a narrow baseband which can be sampled at low speed. Based on the several sampling sequences, the input signals can be reconstructed by compressed sensing (CS) optimization algorithms. However, the classic MWC (C-MWC) still consumes a lot of hardware resources because of its complex structure. Especially when the spectrum is blind, the total sampling rate is required to be four times the Landau rate for joint sparse reconstruction. To solve this problem, this paper proposes alternate MWC (A-MWC). A-MWC replaces the periodic PRBSes with two sets of alternating PRBSes and uses a trigger to synchronize the PRBSes and the sample sequences. Based on a reasonable assumption that the input signals are the wide-sense stationary (WSS) signals which have the same power spectral density (PSD) in each time slice, this paper reduces the requirement the sampling rate for blind joint sparse reconstruction to twice Landau rate successfully. Both simulation and experiment prove that A-MWC reduces the number of branches required for blind reconstruction without reducing the quality of the reconstructed signal.

**INDEX TERMS** Modulated wideband converter, compressed sensing, hardware implementation, cognitive radio, wide-sense stationary signal.

## I. INTRODUCTION

With the rapid development of wireless communication in recent years, the spectrum becomes crucially scarce. However, the spectrum resource is wasted due to it is not fully utilized by primary users (PUs). Cognitive radio (CR) is proposed to improve spectrum utilization by opportunistic sharing the spectrum between PUs and secondary Users (SUs) [1]–[5]. Therefore, SUs not only need to monitor a wide band to ensure sufficient unoccupied spectrum but also need to receive and reconstruct the union of several bands.

Due to the sparseness and randomness of the spectrum processed by SUs, the traditional Nyquist sampling consumes considerable hardware resources, and the sampling signal contains a significant amount of redundant information. Analog compressed sampling is a class of sub-Nyquist sampling structures based on CS theory [3], [6]–[8]. With limited hardware resources, they have the dual capabilities of spectrum sensing and signals reconstruction [9], [10].

In recent years, several compressed sampling structures have been proposed and improved, such as random demodulation [11]–[13], multi-coset sampling [10], [14], MWC [15]–[18] and so on. Random demodulation can sense the discrete spectrum and reconstruct a multi-tone signal, but it is difficult to be compatible with a piecewise continuous multiband spectrum. In spite of the strong application for multi-band signals, the performance of multi-coset sampling structures is also limited by the front-end bandwidths of ADCs and extreme sensitivity of channel mismatch. In [19], Mishali and Elder proposed C-MWC, which ADCs only need to sample the low-pass filtered signal. Benefited from its hardware realizability and natural advantage of processing multi-band signals, this structure is very suitable for CR technologies.

Landau discovered a minimal rate requirement allowing a perfect reconstruction for any sampling system, which is

The associate editor coordinating the review of this manuscript and approving it for publication was Rui Wang.

called Landau rate [20]. Landau rate is equal to the actual frequency occupancy. For an $N$-band signal in which the maximum bandwidth of each band does not exceed $B_w$, the Landau rate is $NB_w$. Mishali and Elder demonstrated that the sample rate need for blind reconstruction by C-MWC is as two times as a Landau rate [10], [21]. As stated, the blind reconstruction algorithm named SBR2 need a sampling rate of 2 $NB_w$, but it isn't a perfect reconstruction in some cases. The method named SBR4 is claimed to be a perfect reconstruction, but the sampling rate of 4 $NB_w$ is needed.For C-MWC, the cost of the hardware resource is positively related to the number of branches. And the number of branches is proportional to the total sampling rate of C-MWC structure. Although it is possible to reduce the number of branches by increasing the sample rate of each branch, the number of branches is still considerable for the hardware implementation, especially blind signal reconstruction [10].

Under the assumption that the received signal is a WSS signal, literature [22]–[24] proposes a single channel MWC for wideband spectrum sensing. Also based on WSS signals, this paper proposes an A-MWC structure that takes into account both wide spectrum sensing and signal reconstruction. As far as we know, almost all existing communication signals are wide-sense stationary, so it is a reasonable and broad assumption. Using two sets of alternating PRBSes as local oscillators sequences, A-MWC successfully reduces the sampling rate required for blind joint spares reconstruction of signals to twice Landau rate without degrading the reconstructed signal quality.

This paper is organized as flow: In Section II, we present the C-MWC structure and the signal processing of C-MWC briefly. Section III described the A-MWC structure and compared the similarities and differences between A-MWC and C-MWC. The simulations based on MATLAB are placed in Section IV. In V, a circuit-level A-MWC is designed and the experimental results are displayed. Finally, Section VI concludes this paper.

## II. THE CLASSICAL MODULATED WIDEBAND CONVERTER

### A. SPARSE MULTI-BAND SIGNAL MODEL

The signals which can be processed by C-MWC must conform to the sparse multi-band signal model, as shown in Fig. 1. In this signal model, $x(t)$ is a continuous time real signal. $x(f)$, the Fourier transformation of $x(t)$ has at most $N$ disjoint sub-bands which distributed in $\mathbb{F}_{Nyq} = [-F_{Nyq}/2, F_{Nyq}/2]$ randomly. $F_{Nyq}$ is the Nyquist frequency and $N$ is an even number due to the conjugate symmetry of the spectrum of the real signals. The bandwidth of each sub-band does not exceed $B_w$ Hz. The signals are considered sparse in frequency domain if thermal noise is ignored.

TABLE 1 summarizes some symbols and their meanings in this paper. Constants, intervals, sets, and variables are written in different formats.

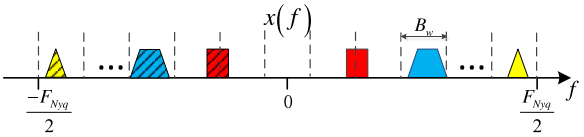


**FIGURE 1.** The signal model of C-MWC.

**TABLE 1.** Symbol description.

| Symbol | Definition |
|---|---|
| $F_{Nyq}$ | Nyquist frequency of input signal |
| $F_s$ | Sampling rate |
| $F_{ct}$ | Cutoff frequency of low pass filter |
| $T_p$ | Period of $p_i(t)$ |
| $F_p$ | $1/T_p$ |
| $P_i$ | One cycle of the $i$-th PRBS |
| $W$ | Number of the bits of $P_i$ |
| $M$ | Number of physical branches |
| $Q_e$ | Expansion factor (is an integer) of the expander, $F_s/F_p$ |
| $Q'_e$ | $Q_e = 2Q'_e + 1$ |
| $N$ | Maximum number of the sub-bands of C-MWC and A-MWC signal model |
| $N_g$ | Maximum number of stationary transmissions in A-MWC signal model, $N = 2N_g$ |
| $B_w$ | Maximal bandwidth of each sub-band of $x(t)$ |
| $L_0$ | The smallest integer greater than $(F_{Nyq} + F_s)/2F_p - 1$ |
| $L$ | $2L_0 + 1$ |
| $D_{fa}$ | Number of false alarm bands allowed by successful support set reconstruction |
| $N_l$ | Length of reconstructed baseband sequences |
| $\mathbb{F}_p$ | Frequency interval $[-F_p/2, F_p/2]$ |
| $\mathbb{F}_S$ | Frequency interval $[-F_s/2, F_s/2]$ |
| $\mathbb{F}_{Nyq}$ | Frequency interval $[-F_{Nyq}/2, F_{Nyq}/2]$ |
| $\mathbb{T}_A$ | The time interval in which $\mathcal{Q}_A$ works; As shown in Fig. 6 |
| $\mathbb{T}_B$ | The time interval in which $\mathcal{Q}_B$ works; As shown in Fig. 6 |
| $\mathcal{S}$ | Support set |
| $\mathcal{Q}$ | The set of the PRBSes of C-MWC |
| $\mathcal{Q}_A$ | The set of the PRBSes which work in $\mathbb{T}_A$ of A-MWC |
| $\mathcal{Q}_B$ | The set of the PRBSes which work in $\mathbb{T}_B$ of A-MWC |
| $\mathcal{N}_+$ | Positive integer set |
| $\mathcal{N}$ | Natural number set |
| $i$ | Index number of the physical branch, $1 \le i \le M$ |
| $l$ | Index number of Fourier coefficients of PRBS, and it is limited to $-L_0 \le l \le L_0$ by the low pass filters |
| $k$ | Index number of sub-branches extended by a physical branch, $-Q'_e \le k \le Q'_e$ |
| $b$ | Index number of the elements of $\mathbf{y}^A(f)$, $1 \le b \le MQ_e$ |

### B. COMPRESSED SAMPLING OF C-MWC

C-MWC is a sub-Nyquist sampling structure with $M$ branches, and its structure is shown in Fig. 2. The input signal $x(t)$ is divided into $M$ branches by a splitter. In $i$-th branch, the divided signal is mixed with a $T_p$-periodic PRBS $p_i(t)$ which alternates between the levels $\pm 1$ for each bit. The symbol $P_i$ represents one cycle of $p_i(t)$, and it contains $W$ bits. C-MWC requires $F_p \ge B_w$, where $F_p = 1/T_p$. Then, the low-pass filter with the cutoff frequency of $F_{ct} = F_s/2$ limits the bandwidth of the mixed signal. An ADC with the sampling rate of $F_s$ behinds the filter to sample the band-limited signal. And the sample sequence is represented as $y_i[n]$. In C-MWC, a total of $M$ PRBSes are required, and they are different from

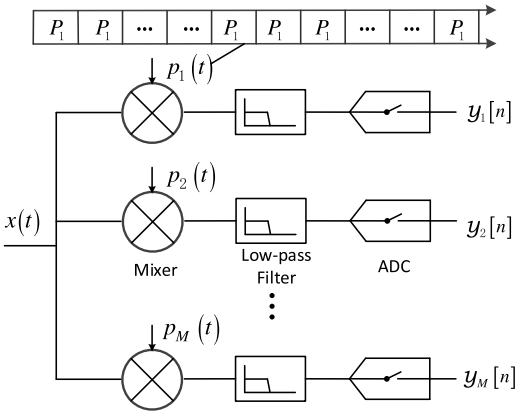


**FIGURE 2.** The structure of C-MWC.

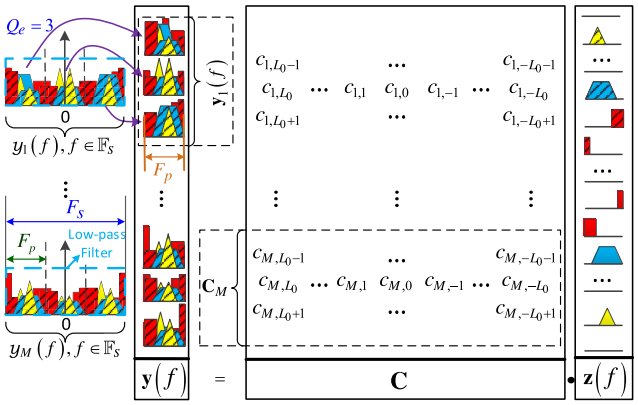


**FIGURE 3.** The spectrum analysis of C-MWC.

each other. These PRBSes are constantly repeated, as shown in Fig. 2. The set of $M$ PRBSes is recorded as $\mathcal{Q}$.

Consider the $i$-th branch. $p_i(t)$ has a Fourier expansion

$$p_i(t) = \sum_{l=-\infty}^{\infty} c_{i,l} e^{j\frac{2\pi}{T_p}lt} \tag{1}$$

where

$$c_{i,l} = \frac{1}{T_p}\int_0^{T_p} p_i(t) e^{-j\frac{2\pi}{T_p}lt} dt \tag{2}$$

When $F_s = F_p$, the discrete-time Fourier transform of the $i$-th band-limited sampling sequence $y_i[n]$ is expressed as

$$y_i(f) = Y_i\left(e^{j2\pi f T_s}\right) = \sum_{l=-L_0}^{+L_0} c_{i,l} x\left(f - lF_p\right), \quad f \in \mathbb{F}_p \tag{3}$$

where $\mathbb{F}_p = [-F_p/2, F_p/2]$ and $L_0 = \lceil \frac{F_{Nyq}+F_s}{2F_p} \rceil - 1$. The operator $\lceil v \rceil$ returns the smallest integer which is greater than (or equal to) $v$. We defined a $L$-length variable $\mathbf{z}(f)$ with the $l$-th element

$$z_l(f) = x(f + lF_p), \quad -L_0 \le l \le L_0, \ f \in \mathbb{F}_p \tag{4}$$

Fig. 3 displays the spectrum of $\mathbf{z}(f)$ which corresponds to the $x(f)$ of Fig. 1. It is convenient to write (3) in matrix as

$$y_i(f) = \mathbf{C}_i \mathbf{z}(f) \tag{5}$$

where $\mathbf{C}_i$ is $L$-length row vector and it is consisted of $c_{i,l}$. This paper uses a Roman, Bold format to write variables and matrix.

Literature [10] proposes a method to reduce the number of physical branches by increasing the ADC sampling rate appropriately. In this method, an expander extends a physical branch into $Q_e$ subbranches, where $Q_e = F_s/F_p$ is the expansion factor. The parameter $Q_e$ is an odd number and $Q_e = 2Q'_e + 1, Q'_e \in \mathcal{N}$, where $\mathcal{N}$ represents the natural number set. The spectrum analysis of an expander with $Q_e = 3$ is shown in Fig. 3. With the expander, (3) is converted to

$$\begin{aligned} y_i(f + kF_p) &= \sum_{l=-L_0}^{+L_0} c_{i,l} x(f + kF_p - lF_p) \\ &= \sum_{l=-L_0}^{+L_0} c_{i,(l+k)} x(f - lF_p) \end{aligned} \tag{6}$$

where $f \in \mathbb{F}_p$ and $-Q'_e \le k \le Q'_e$. The matrix form of (6) is

$$\mathbf{y}_i(f) = \mathbf{C}_i \mathbf{z}(f) \tag{7}$$

where $\mathbf{y}_i(f) = [y_i(f - Q'_e F_p), \ldots, y_i(f), \ldots, y_i(f + Q'_e F_p)]^T$ has $Q_e$ elements and the size of $\mathbf{C}_i$ is $Q_e \times L$. It is worth noting that when $Q'_e = 0$, (7) and (5) are the same.

There are $M$ physical branches in C-MWC structure, so the system can be abstracted into an under-determined equation

$$\mathbf{y}(f) = \mathbf{C}\mathbf{z}(f) \tag{8}$$

where

$$\mathbf{y}(f) = \begin{bmatrix} \mathbf{y}_1(f) \\ \mathbf{y}_2(f) \\ \vdots \\ \mathbf{y}_M(f) \end{bmatrix} \quad \text{and} \quad \mathbf{C} = \begin{bmatrix} \mathbf{C}_1 \\ \mathbf{C}_2 \\ \vdots \\ \mathbf{C}_M \end{bmatrix}.$$

In CS, $\mathbf{y}(f)$ is the observation vector with length of $MQ_e$ and $\mathbf{C}$ is the sensing matrix with the size of $MQ_e \times L$. Fig. 3 also shows how $\mathbf{C}$ is constructed by the Fourier coefficients of PRBSes.

### C. RECONSTRUCTION METHOD

The key of reconstructing the signal is to solve (8). The sparse multi-band signal model requires $N$ non-adjacent sub-bands with the bandwidth $B_w \le F_p$, so $\mathbf{z}(f)$ contains up to $N$ nonzeros for every $f \in \mathbb{F}_p$. That means $\mathbf{z}(f)$ is $N$-sparse for every $f \in \mathbb{F}_p$.

We defined the function ***supp***$(\mathbf{z}(f))$ returns the support set $\mathcal{S}$ which signifies the indices of the nonzeros of $\mathbf{z}(f)$. For any $f$ in $\mathbb{F}_p$, once $\mathcal{S}$ is found in advance, (8) can be simplified as

$$\mathbf{y}(f) = \mathbf{C}_S \mathbf{z}_S(f) \tag{9}$$

where $\mathbf{z}_S(f)$ contains the elements of $\mathbf{z}(f)$ indexed by $\mathcal{S}$ and the other elements are considered to be zeros. Also, $\mathbf{C}_S$ contains the columns of $\mathbf{C}$ indexed by $\mathcal{S}$. As long as $MQ_e \geq N$ is true, (9) is overdetermined or well-defined. Then, $\mathbf{z}_S(f)$ can be calculated by

$$\mathbf{z}_S(f) = \mathbf{C}_S^{\dagger}\mathbf{y}(f) \tag{10}$$

where $\mathbf{C}_S^{\dagger}$ is generalized inverse of $\mathbf{C}_S$.

If the spectrum distribution of $x(f)$ is known in advance, which means that the reconstruction is no-blind, then the support set of $\mathbf{z}(f)$ can be obtained for every $f$ easily. The reconstruction condition $MQ_e \geq N$ means that the total sampling rate is greater than the Landau rate.

When the exact distribution of the signal band is unknown, some CS algorithm is needed to reconstruct the support set, such as $l_0$-norm-based greedy algorithms [25], [25]–[27], $l_1$-norm-based convex optimization [28], sparse Bayesian learning [29], [30], etc. Due to $f$ is continuous, solving (8) is the problem about infinite measurement vectors (IMV). The approach which is to find $\mathbf{z}(f)$ over a dense grid of $\mathbb{F}_p$ is called discrete sparse reconstruction in this paper. Literature [10] and [21] introduced a necessary condition for guaranteeing the uniqueness of reconstruction is that the number of rows of $\mathbf{C}$ is greater than twice the sparsity, ie $MQ_e \geq 2N$. It means that the total sampling rate is greater than twice the Landau rate for blind discrete sparse reconstruction.

However, discrete sparse reconstruction is very complicated and cumbersome. Joint sparse considers the continuous interval as a whole in the issue about sparse, and it is very convenient and efficient to solve an IMV problem. For a collection of vectors $\mathbf{z}(f)$ over a continuous interval $\mathbf{z}(\mathbb{F}_p) = \{\mathbf{z}(f) : f \in \mathbb{F}_p\}$, its support set is defined by

$$\mathcal{S} = \boldsymbol{supp}(\mathbf{z}(\mathbb{F}_p)) = \bigcup_{f\in\mathbb{F}_p} \boldsymbol{supp}(\mathbf{z}(f)) \tag{11}$$

$z(f)$ is $N$-sparse for every $f \in \mathbb{F}_p$, but $\mathbf{z}(\mathbb{F}_p)$ is jointly $2N$-sparse for that each sub-band of $x(f)$ can contribute up to two non-zero elements for $\mathbf{z}(\mathbb{F}_p)$. As shown in Fig.3, the red sub-band of $x(f)$ contributes two non-zeroes to $\mathbf{z}(\mathbb{F}_p)$. For all $f \in \mathbb{F}_p$, $\mathbf{z}(f)$ share this support set, then (9) and (10) are applicable to the entire interval.

Continuous of finite (CTF) block proposed in [10], [21] is applied to find the support set of an infinite measurement vectors. As shown in Fig. 4, CTF block defined a $MQ_e \times MQ_e$ matrix

$$\mathbf{Q} = \int_{f\in\mathbb{F}_p} \mathbf{y}(f)\mathbf{y}^{\mathbf{H}}(f)\, df \tag{12}$$

where the superscript $\mathbf{H}$ signifies the Hermitian transpose. Then, we need to solve for any matrix $\mathbf{V}$ according to $\mathbf{Q} = \mathbf{V}\mathbf{V}^{\mathbf{H}}$ and construct a new equation

$$\mathbf{V} = \mathbf{C}\mathbf{U} \tag{13}$$

Equation (13) is referred to as multiple measurement vectors (MMV) problem which can be solved by some classical CS optimization algorithms [25]–[27], [29]. Literature [10] and [21] prove that the sparsest solution $\mathbf{U}$ of (13) has the same support set $\mathcal{S}$ as $\mathbf{z}(f)$. Therefore, $\mathbf{U}$ is also jointly $2N$-sparse. Similarly, to ensure the uniqueness of the sparse solution, any $4N$ columns of $\mathbf{C}$ must be linearly independent, so $MQ_e \geq 4N$. It means that the total sampling rate for joint sparse reconstruction needs more than 4 times the Landau rate. Although the total sampling rate required is doubled, the joint sparse reconstruction only uses the CS algorithm once to reconstruct the support set. Therefore, joint sparse reconstruction greatly reduces the amount of calculation and is widely used in engineering. Fig. 4 summarizes the process of joint sparse reconstruction of C-MWC.

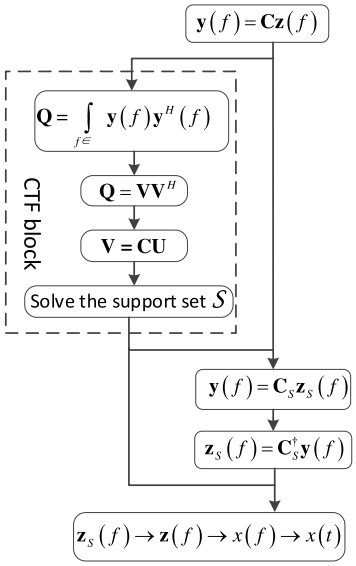


**FIGURE 4.** The flow chart of joint sparse reconstruction of C-MWC.

The minimum total sampling rate required for signal reconstruction of C-MWC is summarized in TABLE 2.

## III. ALTERNATE MODULATED WIDEBAND CONVERTER

As described in the literature [21], the C-MWC structure requires at least twice the Landau rate for blind discrete sparse reconstruction, that means $MQ_e \geq 2N$. But joint sparse reconstruction with more engineering value requires a total sampling rate greater than 4 times the Landau rate.

In this paper, we propose A-MWC structure for processing the WSS signals. As shown in Fig. 5, a trigger which is an uniform square wave is generated to synchronize all the PRBSes and ADCs. And the period of the trigger is determined by the length of sampling window. Unlike MWC, which requires a set of $M$ PRBSes to repeat continuously, A-MWC requires two set of $M$ PRBSes to repeat alternately. When the received signal is a WSS signal, the sampling rate required for blind discrete sparse reconstruction is reduced to the Landau rate. Aslo, the total sampling required for joint sparse reconstruction is reduced to twice the Landau rate. In this section, we introduce the signal model, sampling processing and signal blind reconstruction of A-MWC.

**TABLE 2. Comparison between C-MWC and A-MWC.**

| | | | C-MWC | A-MWC |
|---|---|---|---|---|
| Input Signal | | | Sparse Multi-band Signal | Sparse Multi-band WSS Signal |
| Set of PRBSes | | | $\mathcal{Q}$, containing $M$ PRBSes | $\mathcal{Q}_A$ and $\mathcal{Q}_B$, each containing $M$ PRBSes |
| Transmission Mode of PRBSes | | | $\mathcal{Q}$ repeats in the whole sampling duration | Alternate repetition, $\mathcal{Q}_A$ repeats in $\mathbb{T}_A$, and $\mathcal{Q}_B$ repeats in $\mathbb{T}_B$ |
| Period of PRBSes | | | $T_p$ | $T_p$, whether in $\mathbb{T}_A$ or $\mathbb{T}_B$ |
| Trigger | | | Non | Synchronize PRBS generators and ADCs, and control the switching between $\mathcal{Q}_A$ and $\mathcal{Q}_B$ |
| Method of Signal Reconstruction | | | Fig. 4 | Fig. 7 |
| No-blind | Sensing Matrix | | $\mathbf{C}$ $(MQ_e \times L)$ | $\mathbf{C}^A$ and $\mathbf{C}^B$ $(MQ_e \times L)$ |
| | Discrete Sparse Reconstruction | Sparse Variable | $\mathbf{z}(f)$, $N$-sparse for every $f \in \mathbb{F}_p$ | $\mathbf{z}^A(f)$ and $\mathbf{z}^B(f)$, $N$-sparse for every $f \in \mathbb{F}_p$ |
| | | Number of Sub-branches | $MQ_e \geq N$ | $MQ_e \geq N$ |
| | | Total Sampling Rate | Landau rate | Landau rate |
| | Joint Sparse Reconstruction | Sparse Variable | $\mathbf{z}(f)$, Jointly $2N$-sparse | $\mathbf{z}^A(f)$ and $\mathbf{z}^B(f)$, Jointly $2N$-sparse |
| | | Number of Sub-branches | $MQ_e \geq 2N$ | $MQ_e \geq 2N$ |
| | | Total Sampling Rate | $2\times$ Landau rate | $2\times$ Landau rate |
| Blind | Sensing Matrix | | $\mathbf{C}$ $(MQ_e \times L)$ | $\mathbf{D}(2MQ_e \times L)$ |
| | Discrete Sparse Reconstruction | Sparse Variable | $\mathbf{z}(f)$, $N$-sparse for every $f \in \mathbb{F}_p$ | $\mathbf{P}_x(f)$, $N$-sparse for every $f \in \mathbb{F}_p$ |
| | | Number of Sub-branches | $MQ_e \geq 2N$ | $MQ_e \geq N$ |
| | | Total Sampling Rate | $2\times$ Landau rate | Landau rate |
| | Joint Sparse Reconstruction | Sparse Variable | $\mathbf{z}(f)$, Jointly $2N$-sparse | $\mathbf{P}_x(f)$, Jointly $2N$-sparse |
| | | Number of Sub-branches | $MQ_e \geq 4N$ | $MQ_e \geq 2N$ |
| | | Total Sampling Rate | $4\times$ Landau rate | $2\times$ Landau rate |

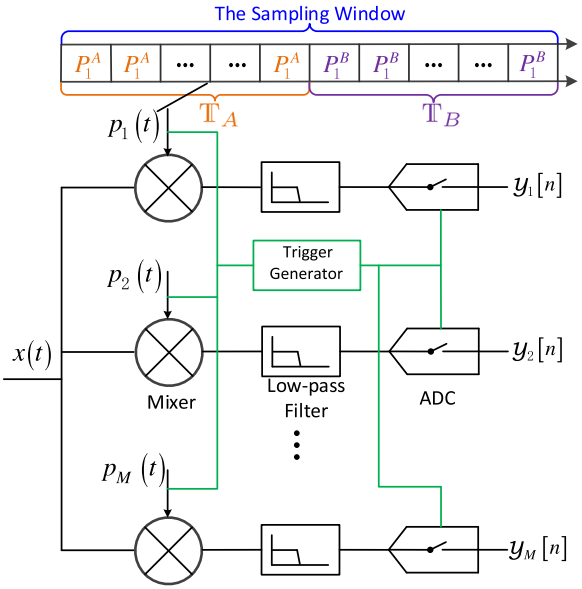


**FIGURE 5. The structure of A-MWC.**

### A. SPARSE MULTI-BAND WSS SINGNAL

Assuming a real-valued continuous-time signal $x(t)$ consists of up to $N_g$ stationary transmissions which are uncorrelated with each other, $x(t)$ can be modeled as

$$x(t) = \sum_{g=1}^{N_g} \beta_g s_g(t). \tag{14}$$

where $s_g(t)$ represent a band-limited wide-sense stationary real signal with zero-mean, and $\beta_g \in \{0, 1\}$ has the power to decide whether the $g$-th transmission is present or not. In the frequency domain, $x(t)$ is demanded to contain $N = 2N_g$ nonadjacent continuous sub-bands that randomly distribute in $[-F_{Nyq}/2, F_{Nyq}/2]$, and the bandwidth of each sub-band is not more than $B_w$ Hz. The symbol $F_{Nyq}$ indicates the Nyquist frequency. Therefore, the effective bandwidth of the signal does not exceed $NB_w$ Hz.

Assume that the input signal is a band-limited zero-mean WSS process which has the same power spectral densitie (PSD) in any time slice [22], [31]. The PSD obeys the function $P_x(f) = \int_{-\infty}^{\infty} x(\tau)x(\tau - t)\exp(-j2\pi f\tau)d\tau$, and (15) is hold.

$$\mathbf{E}\{x(f_1)x(f_2)^{\mathbf{H}}\} = 2\pi P_x(f)\delta(f_1 - f_2) \tag{15}$$

where $\mathbf{E}\{\cdot\}$ signifies the expectation operator.

### B. SAMPLING PROCESSING OF A-MWC

In C-MWC, the $W$-bit PRBSes are always repeated. But in A-MWC, there are two sets of $W$-bit PRBSes, named set $\mathcal{Q}_A$ and set $\mathcal{Q}_B$ respectively. Each set contains $M$ PRBSes, corresponding to $M$ branches.

In fact, due to hardware limitations, the length of the sampling sequences is finite. There is a sampling time window function implicit in signal processing of both C-MWC and A-MWC. The timing of signals in A-MWC are displayed in Fig. 6. As shown, the sampling window is divided into sampling sub-window A and sampling sub-window B, which are correspond to two equal time intervals $\mathbb{T}_A$ and $\mathbb{T}_B$ respectively. In $\mathbb{T}_A$, $\mathcal{Q}_A$ are sent repeatedly with the period of $T_p$, and $P_i^A$ represents a cycle of the PRBS in the $i$-th branch. But in $\mathbb{T}_B$, $\mathcal{Q}_B$ participates in mixing with period of $T_p$, and $P_i^B$

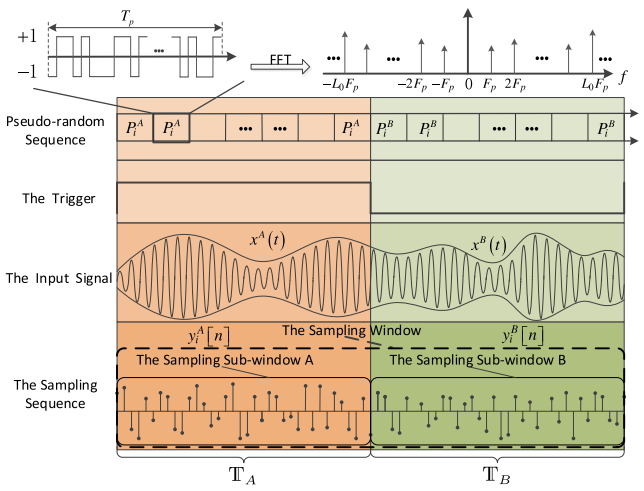


**FIGURE 6.** The timing of signals in A-MWC.

represents a cycle of $p_i^B(t)$. Both $\mathbb{T}_A$ and $\mathbb{T}_B$ are preferably integer multiples of $T_p$.

A-MWC considers the input signal $x(t)$ separately in the two time intervals $\mathbb{T}_A$ and $\mathbb{T}_B$, and two signals are defined as

$$x^A(t) = x(t), \quad t \in \mathbb{T}_A \tag{16}$$
$$x^B(t) = x(t), \quad t \in \mathbb{T}_B. \tag{17}$$

And $x^A(f)$ and $x^B(f)$ represent the spectrum of $x^A(t)$ and $x^B(t)$, respectively. Since a WSS signal has a same power spectral densities in any time slice, $x^A(t)$ and $x^B(t)$ have a same PSD function $P_x(f)$.

The sampling sequence matrix $\mathbf{y}[n]$ is also split in time into two parts,

$$\mathbf{y}^A[n] = \mathbf{y}[n], \quad \frac{n}{F_s} \in \mathbb{T}_A \tag{18}$$
$$\mathbf{y}^B[n] = \mathbf{y}[n], \quad \frac{n}{F_s} \in \mathbb{T}_B \tag{19}$$

The trigger synchronizes the PRBSes with the sampling sequences, and its presence guarantees that $\mathbf{y}^A[n]$ and $\mathcal{Q}_A$ are consistent on the timeline. Of course, $\mathbf{y}^B[n]$, and $\mathcal{Q}_B$ are also consistent in $\mathbb{T}_B$.

In $\mathbb{T}_A$, A-MWC is equivalent to a C-MWC with the PRBSes of $\mathcal{Q}_A$. $x^A(t)$ is the input signal, $\mathbf{y}^A[n]$ represents the $M$ sampling sequences. Therefore, an under-determined equation is built like (8).

$$\mathbf{y}^A(f) = \mathbf{C}^A\mathbf{z}^A(f) \tag{20}$$

where $\mathbf{C}^A$ is the sensing matrix composed of Fourier coefficients of the PRBSes of $\mathcal{Q}_A$. The $l$-th element of $\mathbf{z}^A(f)$ is expressed as

$$z_l^A(f) = x^A(f + lF_p), \quad -L_0 \le l \le L_0,\ f \in \mathbb{F}_p \tag{21}$$

In the same way, A-MWC is equivalent to a C-MWC with the PRBSes of $\mathcal{Q}_B$ in $\mathbb{T}_B$. So, (22) and (23) are obtained.

$$\mathbf{y}^B(f) = \mathbf{C}^B\mathbf{z}^B(f) \tag{22}$$

$$z_l^B(f) = x^B(f + lF_p), \quad -L_0 \le l \le L_0,\ f \in \mathbb{F}_p \tag{23}$$

A-MWC is equivalent to two C-MWCs that work alternately in time, and the two C-MWCs which use two different sets of PRBSes are considered to be independent. (20) and (22) are also established separately in their respective time intervals.

### C. RECONSTRUCTION METHOD OF A-MWC

As long as (20) and (22) are solved, the signal $x^A(t)$ and $x^B(t)$ can be successfully reconstructed, then $x(t)$ can also be obtained by simple splicing. A reasonable assumption is that the spectral distribution of the WSS signal does not change in the sampling duration. This means that $x^A(f)$ and $x^B(f)$ have the same distribution of non-zeroes. For every $f \in \mathbb{F}_p$, $\mathbf{z}^A(f)$ and $\mathbf{z}^B(f)$ are both $N$-sparse. As analyzed in Section II-C, both $\mathbf{z}^A(\mathbb{F}_p)$ and $\mathbf{z}^B(\mathbb{F}_p)$ are jointly $2N$-sparse, and they also have the same support set.

If the signal is non-blind, the support set $\mathcal{S}$ can be easily obtained, whether discrete sparse reconstruction or joint sparse reconstruction. With $\mathcal{S}$, (20) and (22) can be simplified like (9).

$$\mathbf{y}^A(f) = \mathbf{C}_S^A\mathbf{z}_S^A(f) \tag{24}$$
$$\mathbf{y}^B(f) = \mathbf{C}_S^B\mathbf{z}_S^B(f) \tag{25}$$

Like C-MWC, no-blind discrete sparse reconstruction requires that the total sampling rate be greater than the Landau rate, (24) and (25) can be solved by generalized inverse matrix, while no-blind joint sparse reconstruction requires a total sampling rate of more than twice the Landau rate.

$$\mathbf{z}_S^A(f) = [\mathbf{C}_S^A]^\dagger\mathbf{y}^A(f) \tag{26}$$
$$\mathbf{z}_S^B(f) = [\mathbf{C}_S^B]^\dagger\mathbf{y}^B(f) \tag{27}$$

Although the sampling rate required for non-blind reconstruction is exactly the same as that of C-MWC, A-MWC can show its advantages in blind reconstruction. If (20) and (22) are solved separately, that is equivalent to solving two independent C-MWCs blindly. As described in Section II-C, blind discrete sparse reconstruction requires a total sampling rate to reach twice the Landau rate, while blind joint sparse reconstruction requires a total sampling rate of 4 times the Landau rate.

An important purpose of this paper is to reduce the total sampling rate required for blind reconstructed signals by exploiting the wide-sense stationarity of the signal. Although $\mathbf{z}^A(f)$ and $\mathbf{z}^B(f)$ have the same distribution of zeroes, (20) and (22) cannot directly solve the support set jointly for $\mathbf{z}^A(f) \neq \mathbf{z}^B(f)$. However, $x^A(t)$ and $x^B(t)$ have the same PSD $P_x(f)$ for the the wide-sense stationarity.

Based on (20), we consider the $b$-th element of $\mathbf{y}^A(f)$.

$$y_b^A(f) = \mathbf{C}_b^A\mathbf{z}^A(f) \tag{28}$$

where $\mathbf{C}_b^A$ represents the $b$-th row of $\mathbf{C}^A$. Do the following calculation

$$\mathbf{E}\{y_b^A(f)[y_b^A(f)]^\mathbf{H}\} = \mathbf{C}_b^A\mathbf{E}\{\mathbf{z}^A(f)[\mathbf{z}^A(f)]^\mathbf{H}\}[\mathbf{C}_b^A]^\mathbf{H} \tag{29}$$

Since $x^A(t)$ is a WSS signal which has the characteristics expressed by (15), $\mathbf{E}\{\mathbf{z}^A(f)[\mathbf{z}^A(f)]^{\mathbf{H}}\}$ is a diagonal matrix.

$$\mathbf{E}\{\mathbf{z}^A(f)[\mathbf{z}^A(f)]^{\mathbf{H}}\} = 2\pi \boldsymbol{diag}(p^x_{-L_0}(f), p^x_{-L_0+1}(f), \ldots, p^x_{L_0}(f)) \quad (30)$$

where $p^x_l(f) = P_x(f + lF_p)$, $-L_0 \le l \le L_0$ and $f \in \mathbb{F}_p$. Then, (29) can be rewritten as

$$\mathbf{E}\{y^A_b(f)[y^A_b(f)]^{\mathbf{H}}\} = 2\pi \sum_{l=-L_0}^{L_0} \mathbf{C}^A_{(b,l)}[\mathbf{C}^A_{(b,l)}]^* p^x_l(f) \quad (31)$$

where $\mathbf{C}^A_{(b,l)}$ represents the elements in the $b$-th row and the $l$-th column of $\mathbf{C}^A$ and the superscript $^*$ indicates the conjugate operation. It is convenient to write (31) as

$$R^A_b(f) = \mathbf{D}^A_b \mathbf{P}_x(f) \quad (32)$$

where $R^A_b(f) = \mathbf{E}\{y^A_b(f)[y^A_b(f)]^{\mathbf{H}}\}$, $\mathbf{D}^A_b$ is a row vector with its $l$-th element being $2\pi \mathbf{C}^A_{(b,l)}[\mathbf{C}^A_{(b,l)}]^*$, and $\mathbf{P}_x(f)$ is a column vector expressed as $\mathbf{P}_x(f) = [p^x_{-L_0}(f), p^x_{-L_0+1}(f), \ldots, p^x_{L_0}(f)]^T$. Because $\mathbf{y}_A(f)$ has a total of $MQ_e$ elements, (32) is expanded in matrix as

$$\mathbf{R}^A(f) = \mathbf{D}^A \mathbf{P}_x(f) \quad (33)$$

where $\mathbf{R}^A(f)$ is $MQ_e$-length column vector with the $b$-th element of $R^A_b(f)$ and $\mathbf{D}$ is a $MQ_e \times L$ matrix. In the same way, (34) is built in time interval $\mathbb{T}_B$.

$$\mathbf{R}^B(f) = \mathbf{D}^B \mathbf{P}_x(f) \quad (34)$$

Because $x^A(t)$ and $x^B(t)$ have a same PSD function $P_x(f)$, (33) and (34) have an identical unknown variable $\mathbf{P}_x(f)$. Combining (33) and (34), we have

$$\mathbf{R}(f) = \mathbf{D}\mathbf{P}_x(f) \quad (35)$$

where $\mathbf{R}(f) = \begin{bmatrix} \mathbf{R}^A(f) \\ \mathbf{R}^B(f) \end{bmatrix}$ and $\mathbf{D} = \begin{bmatrix} \mathbf{D}^A \\ \mathbf{D}^B \end{bmatrix}$. The length of $\mathbf{R}(f)$ is $2MQ_e$ and the size of $\mathbf{D}$ is $2MQ_e \times L$.

Since $x_A(f)$, $x_B(f)$, and $\mathbf{P}_x(f)$ have the same positions of sub-bands, $\mathbf{z}^A(f)$, $\mathbf{z}^B(f)$ and $\mathbf{P}_x(f)$ also have the same distribution of the non-zeroes. Therefore, for every $f \in \mathbb{F}_p$, $\mathbf{P}_x(f)$ is $N$-sparse, while $\mathbf{P}_x(\mathbb{F}_p)$ are jointly $2N$-sparse. By using the same CS algorithm for solving (8), the support set $\mathcal{S}$ of $\mathbf{P}_x(f)$ can be obtained by solving (35). With $\mathcal{S}$, (20) and (22) becomes non-blind reconstruction. The Fig. 7 summarizes the flow of blind joint sparse reconstructed by A-MWC.

TABLE 2 compares the differences between A-MWC and C-MWC. The input signal of C-MWC is sparse multi-band signal, while A-MWC emphasizes the wide stationarity of signal. C-MWC with $M$ branches requires only one set of PRBSes ($\mathcal{Q}$, containing $M$ PRBSes), which is repeated with the period of $T_p$ in the whole sampling duration. However, A-MWC with $M$ branches requires two set of PRBSes, $\mathcal{Q}_\mathcal{A}$ and $\mathcal{Q}_\mathcal{B}$, each of which contains $M$ PRBSes. Moreover, $\mathcal{Q}_\mathcal{A}$ repeats in $\mathbb{T}_A$ with the period of $T_p$, while $\mathcal{Q}_\mathcal{B}$ repeats in $\mathbb{T}_B$ with the period of $T_p$. A-MWC need a trigger to synchronize $\mathbf{y}^A[n]$ and $\mathcal{Q}_A$ in $\mathbb{T}_A$. Of course, $\mathbf{y}^B[n]$ and $\mathcal{Q}_B$ are also synchronized. The signal reconstruction processes of C-MWC and A-MWC are also different and the processes are shown in Fig. 4 and Fig. 7, respectively.

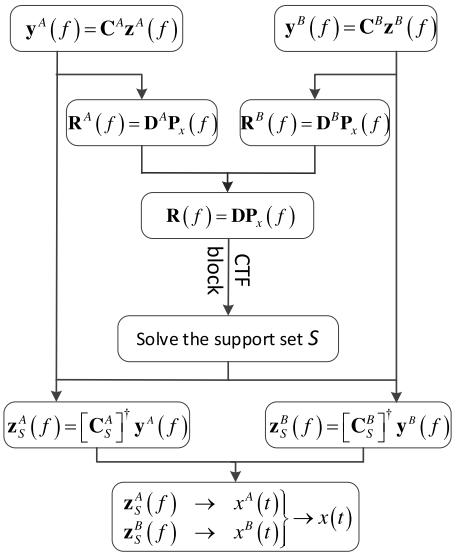


**FIGURE 7.** The signal processing flow chart of A-MWC.

For a C-MWC with $M$ branches, the underdetermined equation (8) has $MQ_e$ rows. However, the undetermined equation (35) constructed by A-MWC with $M$ branches has $2MQ_e$ rows. And their unknown variables $\mathbf{z}(f)$ and $\mathbf{P}_x(f)$ have the same length and sparsity (whether discrete sparse or joint sparse). Therefore, blind discrete sparse reconstruction needs the number of rows of (35) to be greater than twice the sparsity ($2MQ_e \ge 2N \Rightarrow MQ_e \ge N$). It means that the total sampling rate is greater than Landau rate. For blind joint sparse reconstruction, solving (35) needs $2MQ_e \ge 4N \Rightarrow MQ_e \ge 2N$, that is, the total sampling rate is greater than twice Landau rate. Whether blind discrete sparse reconstruction or blind joint sparse reconstruction, the total sampling rate required by A-MWC is half that of C-MWC, so A-MWC has obvious advantages in hardware complexity compared to C-MWC.

For an $N$-band signal, C-MWC requires at least $2N$ (or $4N$) sub-branches to construct an underdetermined equation with $2N$ (or $4N$) rows for blind discrete sparse (or joint sparse) reconstruction. And A-MWC requires at least $N$ (or $2N$) sub-branches to construct an underdetermined equation with $2N$ (or $4N$) rows for blind discrete sparse (or joint sparse) reconstruction. Therefore, the matrix size required to reconstruct the $N$-band is the same whether A-MWC or C-MWC. The CS optimization algorithm for reconstructing the support set plays an absolutely dominant role in the cost of signal reconstruction. But the calculation cost of this part of C-MWC and A-MWC is the same.Therefore, the computational cost of A-MWC is higher than that of C-MWC, but the increase is slight.

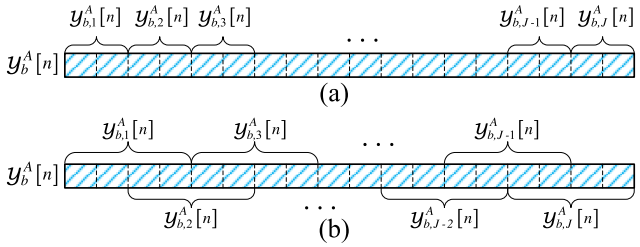


**FIGURE 8.** Schematic of (a) uniform division and (b) moving uniform division.

## IV. SIMULATION

In this section, the estimation method of $\mathbf{E}\{y_b^A(f)[y_b^A(f)]^{\mathbf{H}}\}$ is displayed. We define two criteria that the support sets are considered to be reconstructed effectively. An A-MWC and a C-MWC are built in MATLAB, and the simulation results are also shown in this section.

### A. ESTIMATED METHOD OF EXPECTATION

In A-MWC, the sampling sequences are divided into two parts by the two sampling sub-windows. In their respective sampling sub-windows, (20) and (22) are easily established by the method of C-MWC. To establish (35) successfully, the expectation $\mathbf{E}\{y_b^A(f)[y_b^A(f)]^{\mathbf{H}}\}$ needs to be estimated.

The estimation method is shown here. We transform $y_b^A(f)$ into $y_b^A[n]$ by the inverse fast Fourier transform (IFFT) first. Then, $y_b^A[n]$ is divided into $J$ frames and the $j$-th frame is denoted as $y_{b,j}^A[n]$. The symbol $y_{b,j}^A(f)$ denotes the spectrum of $y_{b,j}^A[n]$. $\mathbf{E}\{y_b^A(f)[y_b^A(f)]^{\mathbf{H}}\}$ can be estimated by statistical average

$$\mathbf{E}\{y_b^A(f)[y_b^A(f)]^{\mathbf{H}}\} = \frac{1}{J}\sum_{j=1}^{J} y_{b,j}^A(f)[y_{b,j}^A(f)]^{\mathbf{H}} \tag{36}$$

A large $J$ value is needed to ensure the accuracy of the estimate. But $y_b^A[n]$ is a finite length sequence. If it is divided equally into $J$ frames as described in Fig. 8(a), the length of each frame $N_j$ may not be sufficient to describe the basic characteristics of the signal. To solve the contradiction between $J$ and $N_j$, we divide $y_b^A[n]$ in the way of moving window, as shown in Fig. 8(b). By controlling the step-length, this method can obtain the appropriate $J$ and $N_j$.

Since the expectations are estimated by statistical average, a long sampling duration is required to obtain enough samples. Although the moving average shown in Fig. 8(b) can somewhat reduce the requirement of sampling points for estimation, a long sampling duration is still recommended.

### B. RECONSTRUCTION OF SUPPORT SET

When the signal is blind, CS optimization algorithms are used to reconstruct the support set. We define two criteria to determine whether the support set is effectively reconstructed, named perfect support set reconstruction and successful support set reconstruction.

When the estimated support set $\mathcal{S}_{est}$ is identical to the actual support set $\mathcal{S}_{act}$, then it is a perfect support set reconstruction.

$$\mathcal{S}_{est} = \mathcal{S}_{act} \tag{37}$$

Perfect reconstruction is a very strict criterion. The response of the CS receiver to the input signal is a very complex nonlinear process, and the boundaries of the sub-bands are difficult to accurately divide. Usually, the reconstruction algorithm sets a looser iterative termination condition to avoid the elements of $\mathcal{S}_{act}$ from being missed, although the false alarm bands may be increased [16], [29]. So we defined successful support set reconstruction as

$$\begin{cases} \mathcal{S}_{act} \subseteq \mathcal{S}_{est} & \text{(38a)} \\ \boldsymbol{num}(\mathcal{S}_{est}) - \boldsymbol{num}(\mathcal{S}_{est}) \le D_{fa} & \text{(38b)} \end{cases}$$

where $\boldsymbol{num}(\mathcal{S})$ represents the number of elements of $\mathcal{S}$. (38ba) guarantees that all elements of $\mathcal{S}_{act}$ are not missing. $D_{fa}$ of (38bb) constrains the number of false alarm bands allowed by successful reconstruction. Due to the conjugate symmetry of the spectrum, the false alarm bands are also present in pairs. So $D_{fa}$ is generally set to even. For example, the support set of a three-carrier real signal is $\mathcal{S}_{act} = \{-64, -51, -47, -46, 46, 47, 51, 64\}$. If $\mathcal{S}_{est} = \{-64, -51, -47, -46, -17, 17, 46, 47, 51, 64\}$, then the bands of the false alarm are $\{-17, 17\}$. Although it is not a perfect reconstruction, the reconstruction is still considered a successful reconstruction with $D_{fa} = 2$.

However, too many false alarm bands can degrade the receiver's reputation for spectrum sensing. According to the number of sub-bands of the input signal, it is necessary to set an appropriate $D_{fa}$ to balance the detection probability and the false alarm probability. In our paper, $D_{fa} = 0$ is set for double-carrier real signal and $D_{fa} = 2$ is set for three-, four-, and five-carrier real signals. For the real signals with more than five carriers, $D_{fa} = 4$ is set. In this paper, the number of carriers only calculates positive frequencies, for example, the number of sub-bands of a four-carrier real signal is $N = 8$.

### C. SIMULATION SETTING

A system with A-MWC structure is designed in MATLAB and TABLE 3 shows the design parameters. The A-MWC has 5 branches with $Q_e = 5$, so both $\mathbf{C}^A$ and $\mathbf{C}^B$ have a size of $25 \times 155$. The sensing matrix is calculated from the Fourier coefficients of 10 PRBSes. Both the mixers and the low-pass filters are ideal. To simplify the operations, the FFT replaces the DTFT in both simulations and experiments. The number of sampling points determines the spectrum resolution of FFT. Whether C-MWC or A-MWC, we recommend a long sampling duration so that FFT has enough points to achieve satisfactory resolution. In the simulation, the sampling window contains 20,000 sampling points, so the sampling duration is 100 us. And the two sample sub-windows each containing 10,000 points are divided according the timeline, so the length of both $\mathbb{T}_A$ and $\mathbb{T}_B$ is 50 us. $\mathcal{Q}_{\mathcal{A}}$ and $\mathcal{Q}_{\mathcal{B}}$ repeat 2000 cycles in $\mathbb{T}_A$ and $\mathbb{T}_B$, respectively.

**TABLE 3. Design parameters of A-MWC and C-MWC in simulation and experiment.**

| Design Parameter | Simulation Value | | Physical Value | |
|---|---|---|---|---|
| | C-MWC | A-MWC | C-MWC | A-MWC |
| $F_{Nyq}$ | 6 GHz | 6 GHz | 6 GHz | 6 GHz |
| $M$ | 5 | 5 | 3 | 3 |
| $Q_e$ | 5 | 5 | 5 | 5 |
| $F_s$ | 200 MHz | 200 MHz | 240 MHz | 240 MHz |
| $B_w$ | 40 MHz | 40 MHz | 40 MHz | 40 MHz |
| The Rate of PRBSes | 6.2 Gbps | 6.2 Gbps | 6.4 Gbps | 6.4 Gbps |
| $W$ | 155 bits | 155 bits | 160 bits | 160 bits |
| $F_p$ | 40 MHz | 40 MHz | 40 MHz | 40 MHz |
| $F_{ct}$ | 100 MHz | 100 MHz | 100 MHz | 100 MHz |
| Sampling Window | 20000 Points | 20000 Points | 65536 Points | 65536 Points |
| Sampling Duration | 100 us | 100 us | 273 us | 273 us |
| $L_0$ | 77 | 77 | 77 | 77 |
| Sensing Matrix | **C** $25 \times 155$ | **D** $50 \times 155$ | **C** $15 \times 155$ | **D** $30 \times 155$ |

When estimating $\mathbf{E}\{y_b^A(f)[y_b^A(f)]^{\mathbf{H}}\}$ using (36), the parameters $J$ and $N_j$ of the moving uniform division are set to 50 and 800, respectively.

As a comparison, a 5-branch C-MWC with $Q_e = 5$ is also built in MATLAB. The PRBSes of C-MWC directly selects $\mathcal{Q}_A$ of A-MWC. The design parameters are also displayed in TABLE 3. The sampling duration is 100 us (20000 sampling points), the PRBSes repeat 4000 cycles in the sampling duration.

In our simulation, a series of multi-band WSS real signals with different signal to noise ratio (SNR) are injected into both A-MWC and C-MWC. The number of carriers of the signals changes from 3 to 8, which means $N$ changes from 6 to 16 with the step of 2. In this simulation, the injected noise is zero-mean Gauss white noise. The signal-to-noise ratio of the input signals varies from $-40$ dB to 40 dB with step of 2 dB. At each number of carriers and each SNR, a hundred of simulations are done. In each simulation, the sub-bands of the injected signal are wideband signals with bandwidth selected from 5 MHz, 10 MHz and 20 MHz randomly, and the carriers are also randomly distributed in [0-3 GHz] while ensuring that all the sub-bands are not adjacent. In each simulation, the signals injected into A-MWC and C-MWC are identical, and the blind joint sparse reconstruction of A-MWC and C-MWC uses an improved orthogonal matching pursuit algorithm.

### D. RESULTS OF SIMULATION

Fig. 9 display the reconstruction probability of support sets varies with SNR and carrier number. As shown, whether A-MWC or C-MWC, the reconstruction probability of the support set increases with the increase of SNR. But A-MWC has better performance than C-MWC in the case of low SNR.

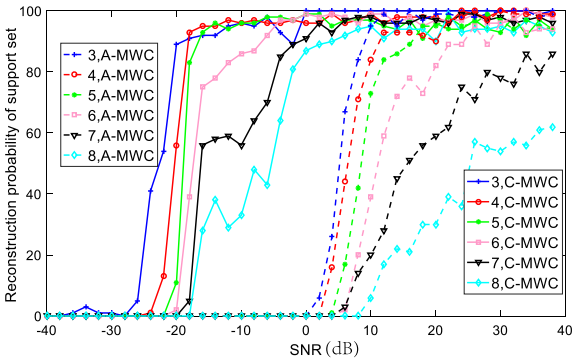


**FIGURE 9. The reconstruction probability of support sets varies with SNR and carrier number.**

When the number of carriers is greater than 7, even if the signal-to-noise ratio is increased to 30 dB, the performance of the support set reconstruction of C-MWC is not satisfactory (reconstruction rate is lower than 80%). However, The probability of reconstructing 8-band signal support set by A-MWC is higher than 90%, when the signal-to-noise ratio is higher than 5 dB.

For an $N$-band signal, the $\mathbf{z}^A(\mathbb{F}_p)$ of C-MWC and the $\mathbf{P}_x(\mathbb{F}_p)$ of A-MWC are theoretically jointly $2N$-sparse. $2N$ only provides a theoretical upper limit, which is to assume that each band provides two non-zeros for $\mathbf{z}^A(\mathbb{F}_p)$ and $\mathbf{P}_x(\mathbb{F}_p)$. However, when the bandwidth of sub-bands is much smaller than $F_p$, each sub-band may only provide one non-zeroes for $\mathbf{z}^A(\mathbb{F}_p)$ and $\mathbf{P}_x(\mathbb{F}_p)$. As shown in Fig. 1, the yellow sub-band contributes a non-zero for $\mathbf{z}^A(\mathbb{F}_p)$ and $\mathbf{P}_x(\mathbb{F}_p)$, while the red sub-band contributes two non-zeroes for $\mathbf{z}^A(\mathbb{F}_p)$ and $\mathbf{P}_x(\mathbb{F}_p)$. The exact sparsity of $\mathbf{z}^A(\mathbb{F}_p)$ and $\mathbf{P}_x(\mathbb{F}_p)$ is between $N$ and $2N$. In addition, the number of rows of (1) and (2) is greater than $4N$ is a strict condition to ensure the uniqueness of the sparse solution. When this condition is broken, the support set may be reconstructed successfully, but its uniqueness is doubtful. The simulation results also confirm that the blind joint sparse reconstruction still has an not bad support set reconstruction rate when the number of sub-bands exceeds the theoretical value ($N = 12$ for A-MWC and $N = 6$ for C-MWC).

Although successful support set reconstruction defined by (38b) allows for some false alarm bands, (26) and (27) are over-determined or well-defined as long as $\boldsymbol{num}(\mathcal{S}_{est}) \leq MQ_e$ is satisfied. Then, the signals of each sub-band can be reconstructed smoothly. Based on this method, the energy of the reconstructed signal on the false alarm band is usually smaller than that of other bands, and the false alarm band can be further determined and removed according to the amplitude of each band. For example, a four-carrier real signal with a SNR of $-18$ dB is injected into the receiver, and the carrier frequencies are 721 MHz (5 MHz), 1203 MHz (20 MHz), 1737 MHz (20 MHz) and 2409 MHz (20 MHz). The values in parentheses represent the bandwidth of sub-bands corresponding to the carrier frequencies. The support set is $\mathcal{S}_{act} = \{-65, -44, -43, -30, -18, 18, 30, 43, 44, 65\}$,

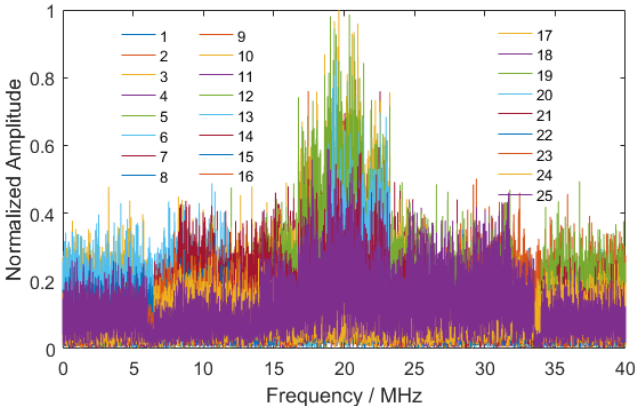


**FIGURE 10.** The normalized amplitude of $\mathbf{y}^A(f)$.

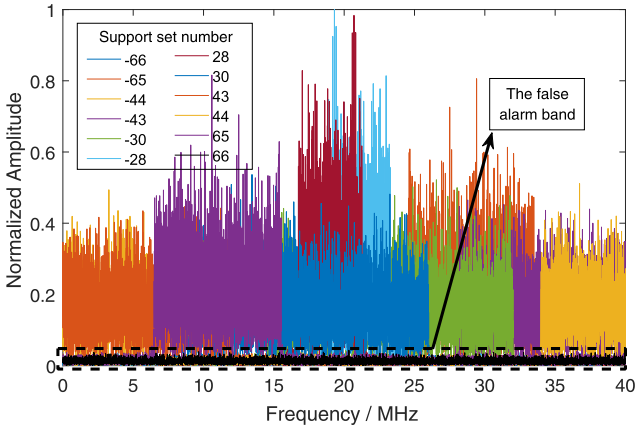


**FIGURE 11.** The normalized amplitude of $\mathbf{z}_S^A(f)$.

but the support set estimated by our CS algorithm is $\mathcal{S}_{est} = \{-66, -65, -44, -43, -30, -18, 18, 30, 43, 44, 65, 66\}$. Obviously, the false alarm bands are $\{-66, 66\}$. When $D_{fa} = 2$, the support set satisfies (38b), so the reconstruction is effective. Fig. 10 display the normalized amplitude of $\mathbf{y}^A(f)$, and the number in the legend indicates the number of the sub-branch of the CS receiver. $\mathbf{z}_S^A(f)$ reconstructed from $\mathcal{S}_{est}$ is shown in Fig. 11. The black spectrum circled by the black imaginary box in the Fig. 11 represents the amplitude allocated to the false alarm band. By calculation, only 0.33 % of the total power is allocated in the false alarm bands in this example. Therefore, we can we can further remove the false alarm bands $\{-66, 66\}$ from $\mathcal{S}_{est}$. A more accurate signal can be reconstructed by the updated support set. Of course, the power weight of the false alarm band will increase as the SNR deteriorates. Therefore, the method of identifying the false alarm bands based on the powers of reconstructed sub-bands can be used as an auxiliary means of reconstructing the signal.

## V. EXPERIMENT

We also designed a circuit-level CS receiver which can switch between A-MWC and C-MWC. In this section, experimental results will be displayed.

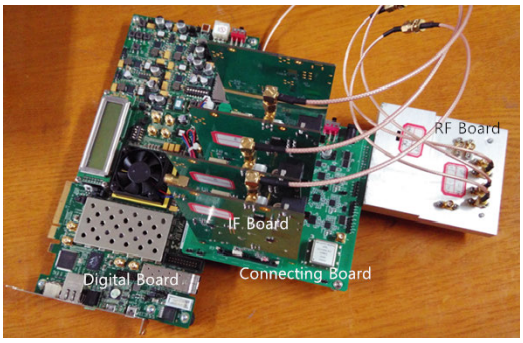


**FIGURE 12.** The photo of our CS receiver.

**TABLE 4.** The PRBSes in hexadecimal form.

| Branch | $\mathcal{Q}_A$ | $\mathcal{Q}_B$ |
|---|---|---|
| 1 | AF82ADF71415CDAC558D<br>EC872B2B2BCB932A2D60 | D4536CB1EED96B0D85EB<br>A744A65BBD8A0BD7E295 |
| 2 | 6354FA923D2327A2EDA6<br>8E26B50EDD898AEE7708 | 9EAB6299BDF89550B53D<br>CB65464F2DE3137CA28D |
| 3 | 87ABAFB723476D9C35D8<br>E547FC80E6D6B7E52C5D | 420FFE0D15535096376D<br>B08A1349D488FA539B08 |

### A. EXPERIMENTAL PLATFORM

The hardware circuit of a CS receiver is shown in the Fig. 12. In this paper, both A-MWC and C-MWC are implemented by this platform. Our CS receiver includes an RF board, three IF boards, an interface converting board and an FPGA (Field Programmable Gate Array) development board. The hardware implementation of this CS receiver is described in detail in [32]. The software ChipScope is responsible for exporting the sample data from FPGA, and the signal is blindly reconstructed in MATLAB.

This hardware platform can receive signals whose spectrum is randomly distributed in [−3 GHz, 3 GHz]. Whether A-MWC or C-MWC, the Nyquist frequency $F_{Nyq}$ is 6 GHz. This hardware platform has three physical branches ($M = 3$), and each physical branch can be expanded to five sub-branches by expander ($Q_e = 5$). The PRBSes with the rate of 6.4 Gbps are generated by the GTX transceiver of Xilinx company's Virtex-7 FPGA VC707 Evaluation Kit. Some of the main parameters of the CS receiver are shown in TABLE 3.

Because in the two time intervals of $\mathbb{T}_A$ and $\mathbb{T}_B$, (20) and (22) are independently constructed in the way of C-MWC structure, and the subsequent operations are only mathematical processing. In theory, the criterion for selecting PRBSes for A-MWC is the same as that for C-MWC. There is no additional requirement. Two sets of 160-bit PRBSes of A-MWC are given in the TABLE 4 in hexadecimal form. C-MWC uses the PRBSes of $\mathcal{Q}_A$ in the experiment.

It's worth noting that the sample rate 240 MHz is larger than twice the cutoff frequency (100 MHz) of the low-pass filter. Because the low-pass filters in objective circuits are not ideal, the descending edge of its frequency response is not steep. In order to reduce the effect of out-of-band information, we have properly increased the sampling frequency

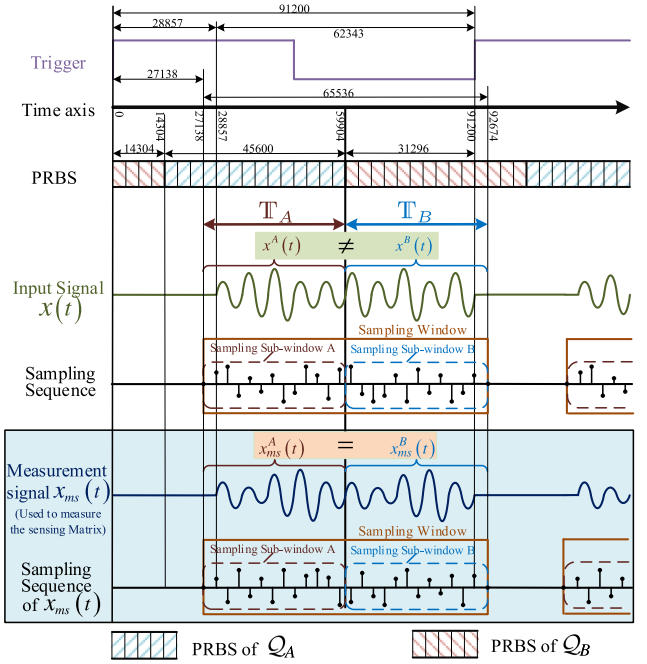


**FIGURE 13.** The timing of signals of our CS receiver based on A-MWC structure.

of the ADC. The sampling sequence is then filtered by a well-performing digital filter before being used to reconstruct the signal.

The transmission time and response time of each chip causes a fixed time delay between all the signals. The timing of some main signals in the receiver is shown in the Fig. 13. A long sampling duration is recommended for FFT to have sufficient spectral resolution and for the estimated $\mathbf{E}\{y_b^A(f)[y_b^A(f)]^{\mathbf{H}}\}$ to be accurate enough. But due to the limit of the buffers of the FPGA, the maximum sampling point of each physical branch is eventually set to 65536. That is to say, the length of the sampling duration is 273.067 us. For C-MWC, PRBSes repeat 10,922 cycles in the sampling duration. For A-MWC, the sampling sub-window A contains 32766 sampling points, the length of $\mathbb{T}_A$ is 136.525 us, and $\mathcal{Q}_A$ repeated 5461 cycles. The sampling sub-window B contains 32770 sampling points. The last four sampling points are discarded in signal reconstruction because they do not contain information in our experiment. The length of $\mathbb{T}_B$ is also 136.525 us, and $\mathcal{Q}_B$ repeated 5461 cycles.

The vector signal generator used in the experiment is SMW200A from Rhode & Schwartz company. After measurement and estimation, the time delay between the rising edge of a trigger generated by FPGA and the beginning of signal generated by vector signal generator is about 120.24 us (about 28857 sampling points at 240 MHz sampling rate), as shown in Fig. 13. In order to make a sufficiently long sampling sequence which containing information fall into the sampling window, the time delay between the trigger signal and the sampling window is set to 113.075 us (27138 sampling points at 240 MHz sampling rate). In this experiment,

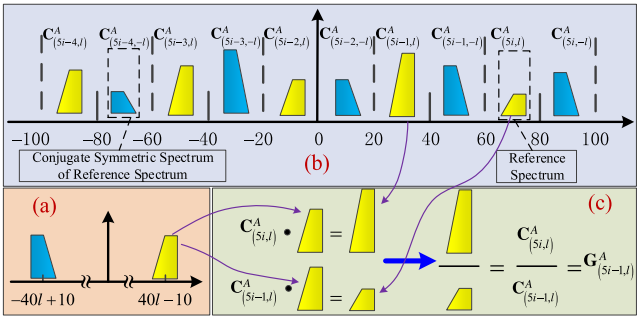


**FIGURE 14.** (a) The spectrum of $x^A_{ms}(t)$. (b) Spectrum of the sampling sequence of a branch. (c) Calculation of relative sensing matrix.

the trigger is set to a square wave with a period of 380 us (91200 sampling points at 240 MHz sampling rate). The time difference between the rising edge of the trigger signal and the time point of switching PRBSes is 59.6 us (14304 sampling points at 240 MHz sampling rate).

### B. MEASUREMENT OF THE SENSING MATRIX

For a hardware-implemented CS receiver, mixing response and channel response are unavoidable due to the non-ideal characteristics of the device. PRBSes with a rate up to several Gbps also suffer from waveform distortion in the process of generation and transmission [33]–[37]. To correct these non-ideal factors, signal reconstruction used the relative sensing matrix measured by some synchronously known signals. A detailed method proposed by us to measure the relative sensing matrix is published in [33].

However, [33] is based on C-MWC, and the measurement method requires a slight change to match A-MWC. In the experiment, 5 MHz wideband synchronously signals were selected as the measurement signals $x_{ms}(t)$. The timing of the measurement signal, trigger, and PRBSes of the A-MWC is shown in Fig. 13. The measurement signal is also split into two parts in time, denoted as $x^A_{ms}(t)$ and $x^B_{ms}(t)$. But the measurement signal needs to guarantee $x^A_{ms}(t) = x^B_{ms}(t)$. So, $x_{ms}(t)$ is a combination of two identical signals in time.

Since the DC blocking capacitor prevents the spectrum in $[-F_p/2, F_p/2]$ ($F_p = 40$ MHz) from entering the circuit-level MWC, the 0-th column of $\mathbf{C}^A$ and $\mathbf{C}^B$ is set to zero. Two columns of elements of $\mathbf{C}^A$ and $\mathbf{C}^B$ can be obtained for each measurement, so a total of $L_0 = 77$ measurements are needed in our platform. At the $l$-th measurement, the carrier of $x_{ms}(t)$ is set to $(40l - 10)$ MHz, the $-l$-th and $l$-th column of $\mathbf{C}^A$ and $\mathbf{C}^B$ will be calculated.

After the bandwidth and carrier of $x_{ms}(t)$ are set as described above, the spectrum of $x_{ms}(t)$ does not alias after mixing and low-pass filtering. The spectrum of $x^A_{ms}(t)$ is shown in Fig.14(a). In $\mathbb{T}_A$ of the $l$-th measurement, the spectrum of the sample sequence of the $i$-th branch is shown in Fig. 14(b). In Fig.14(b), we can see 10 non-overlapping spectral segments, which are the weighted copies of the two sub-bands of $x^A_{ms}(f)$. And these weights are the elements of the $l$-th and $-l$-th columns of $\mathbf{C}^A_i$. In $\mathbb{T}_A$, a total of 30 such

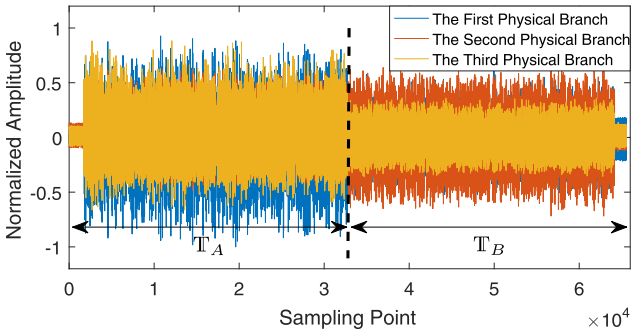


**FIGURE 15.** The sampling sequences of three physical branches of A-MWC.

spectrum copies can be obtained for the three branches. Similarly, in the time interval $\mathbb{T}_B$ of the $l$-th measurement, we can also get 30 such spectrum copies which weights the elements of the $l$-th and $-l$-th columns of $\mathbf{C}^B$. Because $x^A_{ms}(t) = x^B_{ms}(t)$, the spectrum $x^A_{ms}(f) = x^B_{ms}(f)$. So, the prototypes of the spectrum copies are the same whether in $\mathbb{T}_A$ or $\mathbb{T}_B$. After 77 measurements, all the elements of $\mathbf{C}^A$ and $\mathbf{C}^B$ (except the 0th column) will get a spectrum copy of their own. As shown in Fig.14(c), we arbitrarily select a spectrum copy as the reference spectrum, and then calculate the ratios of all the spectrum copies of both $\mathbf{C}^A$ and $\mathbf{C}^B$ to the reference spectrum (or its conjugate symmetric spectrum). As shown in Fig.14(c), the two matrices $\mathbf{G}^A$ and $\mathbf{G}^B$ formed by those ratios are the relative sensing matrix. $\mathbf{G}^A$ and $\mathbf{G}^B$ are essentially normalized $\mathbf{C}^A$ and normalized $\mathbf{C}^B$. $\mathbf{G}^A$ and $\mathbf{G}^B$ are completely equivalent to $\mathbf{C}^A$ and $\mathbf{C}^B$, when reconstructing signals [33].

### C. EXPERIMENTAL RESULT

In our experiment, four multi-carrier wideband real signals are injected into the A-MWC and C-MWC. The carrier frequency, bandwidth, and power of each sub-band of the signal are displayed in TABLE 5. In this paper, we use normalized mean square error (NMSE) to measure the similarity of the reconstructed baseband $x_{BR}[n]$ to the original beseband $x_{BO}[n]$. The NMSE is defined by

$$NMSE = 10\lg \frac{\sum_{n=1}^{N_l} |x_{BR}[n] - x_{BO}[n]|^2}{\sum_{n=1}^{N_l} |x_{BO}|^2} \tag{39}$$

where $N_l$ is the length of the baseband sequences.

A 5 MHz dual-carrier WSS signal is injected into A-MWC and C-MWC separately, and its carrier frequencies are 1990 MHz and 2151 MHz. Both A-MWC and C-MWC reconstruct the support set perfectly. Fig. 15 shows the sampling sequences of three physical branches of A-MWC. In this figure, we can clearly observe that the sample sequences are divided into two segments because A-MWC uses different PRBSes in $\mathbb{T}_A$ and $\mathbb{T}_B$. Fig. 16 shows the normalized amplitude $\mathbf{z}^A_S(f)$ which is reconstructed by the signal recovery algorithm. It is noteworthy that the two subbands are partially aliased after mixing.

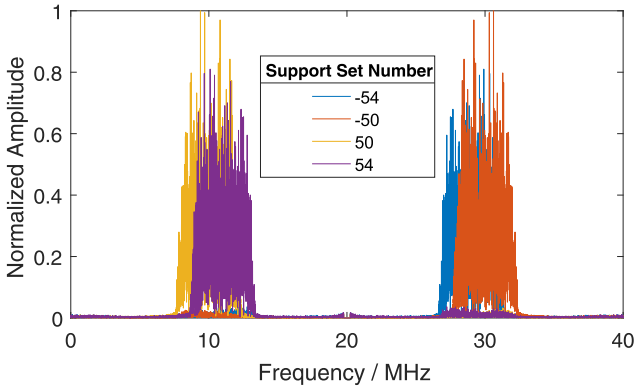


**FIGURE 16.** The normalized amplitude of $\mathbf{z}^A_S(f)$ when A-MWC is injected into a dual carrier signal.

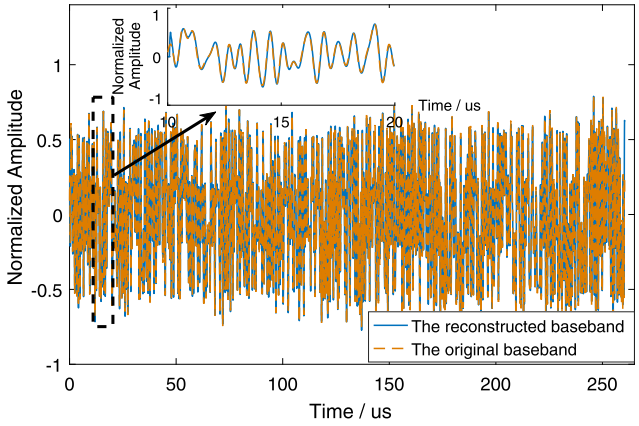


**FIGURE 17.** The comparison of normalized amplitude between reconstructed baseband (1990 MHz) and original baseband.

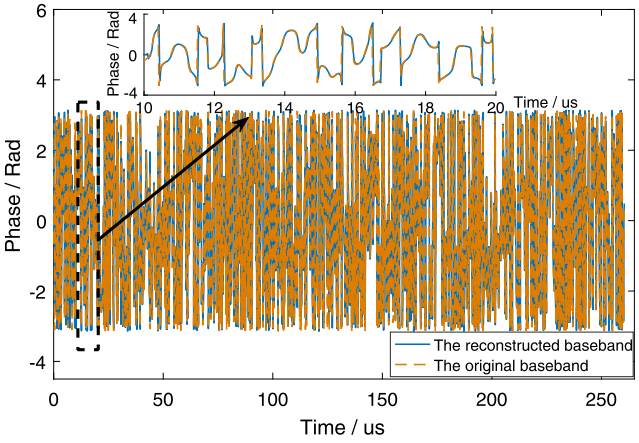


**FIGURE 18.** The comparison of phase between reconstructed baseband (1990 MHz) and original baseband.

After $\mathbf{z}^A_S(f)$ and $\mathbf{z}^B_S(f)$ are obtained, we reconstruct the two basebands separately. Comparing the two reconstructed basebands with the original basebands, NMSE of $-22.63$ dB (1990 MHz) and $-21.47$ dB (2151 MHz) are obtained separately. Fig. 17 and Fig. 18 compare the amplitude and phase of the reconstructed baseband (1990 MHz) with original baseband, respectively.

**TABLE 5. Summary and comparison of experimental results.**

| | | Dual carrier | | | | Three carrier | | | Four carrier | | | |
|---|---|---|---|---|---|---|---|---|---|---|---|---|
| Carrier frequency (MHz) | | 5 | 5 | 5 | 5 | 5 | 5 | 5 | 5 | 10 | 5 | 10 |
| Bandwidth (MHz) | | 1990 | 2151 | 2030 | 2070 | 1950 | 1990 | 2150 | 1950 | 1990 | 2150 | 2190 |
| power (dBm) | | -20 | -20 | -20 | -20 | -21 | -21 | -20 | -21 | -21 | -20 | -18 |
| A-MWC | Support Set | Perfect | | Perfect | | Perfect | | | Successful | | | |
| | NMSE(dB) | -22.63 | -21.47 | -23.14 | -22.01 | -18.20 | -19.20 | -20.16 | -17.48 | -16.69 | -16.99 | -15.30 |
| C-MWC | Support Set | Perfect | | Perfect | | Successful | | | Failure | | | |
| | NMSE(dB) | -23.20 | -21.56 | -24.08 | -22.76 | -17.27 | -19.17 | -18.61 | N | N | N | N |

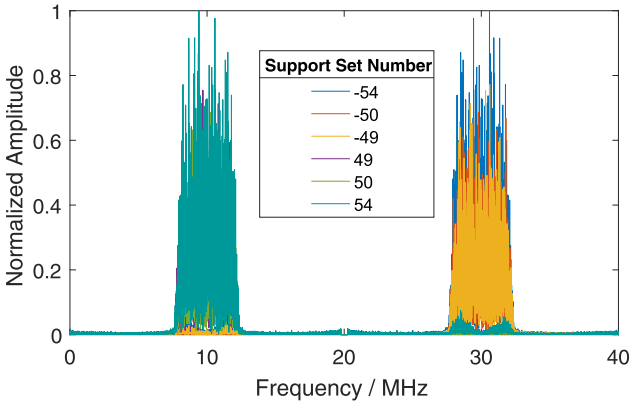


**FIGURE 19.** The normalized amplitude of $\mathbf{z}_S^A(f)$ when A-MWC is injected into the three carrier signal.

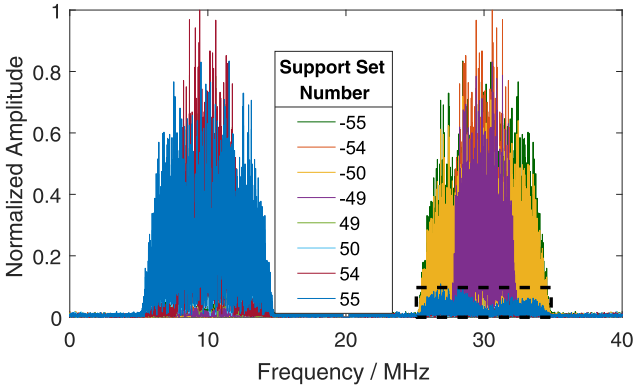


**FIGURE 20.** The normalized amplitude of $\mathbf{z}_S^A(f)$ when A-MWC is injected into the four carrier signal.

A three-carrier real signal with carrier frequencies of 1950 MHz, 1990 MHz and 2150 MHz are injected into A-MWC and C-MWC. The actual support set is $\{-54, -50, -49, 49, 50, 54\}$. A-MWC reconstructs the support set perfectly, but C-MWC reconstructs the support set with a false alarm band $\{-48, 48\}$. The normalized amplitude of the reconstructed $\mathbf{z}_S^A(f)$ is shown in Fig. 19. It can be seen that the three sub-bands completely aliased after mixing. As shown in TABLE 5, comparing the reconstructed baseband with the original baseband, A-MWC has a better NMSE compared to C-MWC. This is mainly due to the fact that the false alarm band of C-MWC separates the energy that should belong to the detection band.

Finally, a four-carrier WSS real signal is injected into A-MWC and C-MWC. This signal contains two 5 MHz real bands (1950 MHz & 2150 MHz) and two 10 MHz real bands (1990 MHz & 2190 MHz). The actual support set is $\{-55, -54, -50, -49, 49, 50, 54, 55\}$. A-MWC reconstructs the support set successfully with false alarm bands $\{-46, 46\}$, but C-MWC failed to reconstruct the support set. The normalized amplitude of the reconstructed $\mathbf{z}_S^A(f)$ is shown in Fig. 20. As the number of carriers and bandwidth of the sub-bands increases, the receiver's response to the input signal becomes very complex. As shown in Fig. 20, the blue spectrum circled by the black dotted frame is incorrectly demodulated to this position. This will cause the reconstructed baseband to deviate from the original baseband, thereby causing a drop in the NMSE.

TABLE 5 summarizes the four sets of experiments in this paper. Under the same total sampling rate, the blind support set reconstruction of A-MWC can adapt more sub-bands than C-MWC. Under the premise that the support set is known, A-MWC and C-MWC can obtain almost the same signal reconstruction quality.

## VI. CONCLUSION

Simulation and experiment prove the feasibility of the A-MWC structure. This structure greatly reduces the complexity of the system without sacrificing quality of signal reconstruction. Under the same total sampling rate, A-MWC can reconstruct more sub-bands than C-MWC blindly. At the same time, our team is committed to the integrated circuit implementation of MWC structure, and a low-cost integrated RF front-end based on a 0.13 $\mu m$ RF CMOS process is designed [38].

## REFERENCES

[1] M. Mishali and Y. C. Eldar, "Wideband spectrum sensing at sub-Nyquist rates [applications corner]," *IEEE Signal Process. Mag.*, vol. 28, no. 4, pp. 102–135, Jul. 2011.

[2] S. K. Sharma, E. Lagunas, S. Chatzinotas, and B. Ottersten, "Application of compressive sensing in cognitive radio communications: A survey," *IEEE Commun. Surveys Tuts.*, vol. 18, no. 3, pp. 1838–1860, 3rd Quart., 2016.

[3] D. Cohen, S. Tsiper, and Y. C. Eldar, "Analog-to-digital cognitive radio: Sampling, detection, and hardware," *IEEE Signal Process. Mag.*, vol. 35, no. 1, pp. 137–166, Jan. 2018.

[4] S. Zheng and X. Yang, "Wideband spectrum sensing in modulated wideband converter based cognitive radio system," in *Proc. 11th Int. Symp. Commun. Inf. Technol. (ISCIT)*, Oct. 2011, pp. 114–119.

[5] A. Ali and W. Hamouda, "Advances on spectrum sensing for cognitive radio networks: Theory and applications," *IEEE Commun. Surveys Tuts.*, vol. 19, no. 2, pp. 1277–1304, 2nd Quart., 2016.

[6] S. Chen and F. Xi, "Quadrature compressive sampling for multiband radar echo signals," *IEEE Access*, vol. 5, pp. 19742–19760, 2017.
[7] D. L. Donoho, "Compressed sensing," *IEEE Trans. Inf. Theory*, vol. 52, no. 4, pp. 1289–1306, Apr. 2006.
[8] S. Qaisar, R. M. Bilal, W. Iqbal, M. Naureen, and S. Lee, "Compressive sensing: From theory to applications, A survey," *J. Commun. Netw.*, vol. 15, no. 5, pp. 443–456, 2013.
[9] M. Mishali, Y. C. Eldar, O. Dounaevsky, and E. Shoshan, "Xampling: Analog to digital at sub-Nyquist rates," *IET Circuits, Devices Syst.*, vol. 5, no. 1, pp. 8–20, Jan. 2011.
[10] M. Mishali and Y. C. Eldar, "From theory to practice: Sub-Nyquist sampling of sparse wideband analog signals," *IEEE J. Sel. Topics Signal Process.*, vol. 4, no. 2, pp. 375–391, Apr. 2010.
[11] S. Smaili and Y. Massoud, "Multi-channel random demodulation for hardware efficient compressive sensing," in *Proc. IEEE 12th Int. New Circuits Syst. Conf. (NEWCAS)*, Jun. 2014, pp. 177–180.
[12] S. Kirolos, J. Laska, M. Wakin, M. Duarte, D. Baron, T. Ragheb, Y. Massoud, and R. Baraniuk, "Analog-to-information conversion via random demodulation," in *Proc. IEEE Dallas/CAS Workshop Design, Appl., Integr. Softw.*, Oct. 2006, pp. 71–74.
[13] S. Smaili and Y. Massoud, "A multi-channel random demodulation reconfigurable receiver," *IEEE Wireless Commun. Lett.*, vol. 3, no. 6, pp. 561–564, Dec. 2014.
[14] R. Venkataramani and Y. Bresler, "Optimal sub-Nyquist nonuniform sampling and reconstruction for multiband signals," *IEEE Trans. Signal Process.*, vol. 49, no. 10, pp. 2301–2313, Oct. 2001.
[15] Y. Zhao and S. Xiao, "Sparse multiband signal acquisition receiver with co-prime sampling," *IEEE Access*, vol. 6, pp. 25261–25269, 2018.
[16] W. Xue, J. Min, X. Gu, and Q. Guo, "Sub-Nyquist spectrum sensing based on modulated wideband converter in cognitive radio sensor networks," *IEEE Access*, vol. 6, pp. 40411–40419, 2018.
[17] Y. Zhao, Y. H. Hu, and J. Liu, "Random triggering-based sub-Nyquist sampling system for sparse multiband signal," *IEEE Trans. Instrum. Meas.*, vol. 66, no. 7, pp. 1789–1797, Jul. 2017.
[18] T. Chen, L. Liu, and X. Huang, "LPI radar waveform recognition based on multi-branch MWC compressed sampling receiver," *IEEE Access*, vol. 6, pp. 30342–30354, 2018.
[19] M. Mishali, Y. C. Eldar, O. Dounaevsky, and E. Shoshan, "Xampling: Analog to digital at sub-Nyquist rates," Dec. 2009, *arXiv:0912.2495*. [Online]. Available: https://arxiv.org/abs/0912.2495
[20] H. J. Landau, "Necessary density conditions for sampling and interpolation of certain entire functions," *Acta Math.*, vol. 117, no. 1, pp. 37–52, 1967.
[21] M. Mishali and Y. C. Eldar, "Blind multiband signal reconstruction: Compressed sensing for analog signals," *IEEE Trans. Signal Process.*, vol. 57, no. 3, pp. 993–1009, Mar. 2009.
[22] W. Sun, Z. Huang, F. Wang, and X. Wang, "Compressive wideband spectrum sensing based on single channel," *Electron. Lett.*, vol. 51, no. 9, pp. 693–695, Apr. 2015.
[23] W. Liu, Z. Huang, X. Wang, and W. Sun, "Design of a single channel modulated wideband converter for wideband spectrum sensing: Theory, architecture and hardware implementation," *Sensors*, vol. 17, no. 5, p. 1035, 2017.
[24] W. Sun, Z. Huang, F. Wang, X. Wang, and S. Xie, "Wideband power spectrum sensing and reconstruction based on single channel sub-Nyquist sampling," *IEICE Trans.Fundamentals Electron., Commun. Comput. Sci.*, vol. E99-A, no. 1, pp. 167–176, 2016.
[25] D. L. Donoho, Y. Tsaig, I. Drori, and J.-L. Starck, "Sparse solution of underdetermined systems of linear equations by stagewise orthogonal matching pursuit," *IEEE Trans. Inf. Theory*, vol. 58, no. 2, pp. 1094–1121, Feb. 2012.
[26] D. Needell and R. Vershynin, "Signal recovery from incomplete and inaccurate measurements via regularized orthogonal matching pursuit," *IEEE J. Sel. Topics Signal Process.*, vol. 4, no. 2, pp. 310–316, Apr. 2010.
[27] D. Needell and J. A. Tropp, "CoSaMP: Iterative signal recovery from incomplete and inaccurate samples," *Appl. Comput. Harmon. Anal.*, vol. 26, no. 3, pp. 301–321, 2009.
[28] M. S. Asif and J. Romberg, "Dynamic updating for $\ell_1$ minimization," *IEEE J. Sel. Topics Signal Process.*, vol. 4, no. 2, pp. 421–434, Apr. 2010.
[29] Y. Gao, Y. Chen, and Y. Ma, "Sparse-Bayesian-learning-based wideband spectrum sensing with simplified modulated wideband converter," *IEEE Access*, vol. 6, pp. 6058–6070, 2018.
[30] Z. Zhang and B. D. Rao, "Sparse signal recovery with temporally correlated source vectors using sparse Bayesian learning," *IEEE J. Sel. Topics Signal Process.*, vol. 5, no. 5, pp. 912–926, Sep. 2011.
[31] A. Papoulis and S. U. Pillai, *Probability, Random Variables, and Stochastic Processes*. New York, NY, USA: McGraw-Hill, 2002, pp. 408–420.
[32] P. Wang, F. You, S. He, and P. Hao "Hardware design of DC-3 GHz compressed sensing receiver based on modulated wideband converter," in *Proc. IEEE Int. RF Microw. Conf. (RFM)*, Dec. 2018, pp. 1–4.
[33] P. Wang, F. You, and S. He, "An improved signal reconstruction of modulated wideband converter using a sensing matrix built upon synchronized modulated signals," *Circuits, Syst., Signal Process.*, vol. 38, no. 7, pp. 3187–3210, Jul. 2019.
[34] E. Israeli, S. Tsiper, D. Cohen, E. Shoshan, R. Hilgendorf, A. Reysenson, and Y. C. Eldar, "Hardware calibration of the modulated wideband converter," in *Proc. IEEE Global Commun. Conf.*, Dec. 2014, pp. 948–953.
[35] L. Chen, J. Jin, and Y. Gu, "A calibration system and perturbation analysis for the modulated wideband converter," in *Proc. IEEE 10th Int. Conf. Signal Process.*, Oct. 2010, pp. 78–81.
[36] Z. Yijiu, L. Ling, Z. Xiaoyan, and D. Zhijian, "Model calibration for compressive sampling system with non-ideal lowpass filter," in *Proc. 12th IEEE Int. Conf. Electron. Meas. Instrum. (ICEMI)*, vol. 2, Jul. 2015, pp. 808–812.
[37] D. Adams, Y. C. Eldar, and B. Murmann, "A mixer front end for a four-channel modulated wideband converter with 62-dB blocker rejection," *IEEE J. Solid-State Circuits*, vol. 52, no. 5, pp. 1286–1294, May 2017.
[38] F. You, P. Shang, and P. Wang, "Design of a low-cost integrated RF front-end for a modulated-wideband-converter based receiver," in *Proc. Asia–Pacific Microw. Conf. (APMC)*, Nov. 2017, pp. 1099–1102.

**PENG WANG** received the B.S. degree in electronic information science and technology from Henan University, Kaifeng, China, in 2012. He is currently pursuing the Ph.D. degree in circuits and systems with the University of Electronic Science and Technology of China (UESTC), Chengdu, China.

He is currently involved in research on architecture design and performance optimization of wideband CS receivers. His research interests include RF/MW receiver systems, undersampling systems, and CS algorithms.

**FEI YOU** (S'07–M'10–SM'18) was born in Chongqing, China, in 1982. He received the bachelor's degree in electronic engineering and the Ph.D. degree in circuits and systems from the University of Electronic Science and Technology of China (UESTC), in 2004 and 2009, respectively, where he is currently an Associate Professor with the School of Electronic Science and Engineering.

From August 2015 to July 2016, he visited the High-Frequency Center with Cardiff University, as an Academic Visitor. His research interest includes high-efficiency power amplifier design and its applications in advanced transmitters. He also carries studies on high-efficiency broadband dc modulators, RF–DC converters, digital Pas, and RF CMOS IC design.

**SONGBAI HE** (M'08–SM'19) received the B.S., M.S., and Ph.D. degrees in electronic engineering from the University of Electronic Science and Technology of China, Chengdu, China, in 1995, 1998, and 2003, respectively.

In 2004, he visited Chiba University, Chiba, Japan, where he was involved in the research of high-efficiency switch-mode power amplifiers. In 2005, he returned to the University of Electronic Science and Technology of China, where he is currently a Professor. His current research plan of broadband high-efficiency linear transmitter was supported by the Hi-Tech Research and Development Program of China. His research interests include RF/MW circuits and systems, frequency synthesis, wireless communication, and nonlinear dynamic systems.